



Downshifting photoluminescence of Erbium doped NaSrZrO₃ for solid-state lighting

A. Nathan-Abutu^{a,b}, I. Ahemen^b, R.E. Kroon^c, A. Reyes-Rojas^{a,*}

^a Materials Science Department, Centro de Investigacion en Materiales Avanzados, S.C., Miguel de Cervantes 120, Complejo Industrial Chihuahua, Chihuahua, CHIH 31109, Mexico

^b Department of Physics, Federal University of Agriculture, P.M.B. 2373, Makurdi, Benue State, Nigeria

^c Department of Physics, University of the Free State, P.O Box 339, Bloemfontein 9300, South Africa

ARTICLE INFO

Keywords:

Photoluminescence
Solid-state lighting
Downshift PL
NaSrZrO₃:Er³⁺ nanophosphor
Perovskite

ABSTRACT

The synthesis of novel nanophosphors exhibiting unique morphologies with high purity, stability, eco-friendliness, and a high color rendering index is crucial to meet the demands of contemporary solid-state lighting energy devices. In this investigation, we successfully synthesized Na_{0.2}Sr_{0.9-x}ZrO₃:xEr³⁺ perovskite nanophosphors. All samples manifested an orthorhombic structure. The crystallite size was observed to increase with rising concentrations of Er³⁺. The optical band gap exhibited a range of 5.19 eV to 5.36 eV with increments in doping concentration, signifying alterations in the lattice constants attributable to crystalline disorder. The downshifting PL spectra revealed both host emission bands and dopant (Er³⁺) emission lines. The violet – blue band was attributed to crystalline disorder while the red emission band was assigned to octahedra tilting disorder in the perovskite. The presence of Er³⁺ ion lines at 523 and 546 nm produced intense green light, as depicted in the CIE chromaticity diagram for all doped samples. The study affirms that the phosphors synthesized in this research possess potential for application in the development of visible green lamps for optical display devices and solid-state lighting.

1. Introduction

The field of nanomaterials is proving highly promising and attractive for technological advancements in the 21st century. This assertion stems from extensive research and synthesis of materials at the nanometer scale, typically ranging between 1 and 100 nm. Materials within this dimension exhibit physical and chemical properties that hold significant promise for future technological applications, particularly in the realm of semiconductors. Consequently, nanophosphors demonstrate the capability to yield distinctive and crucial optical properties, making them valuable for the development of novel lighting technologies.

Nanophosphors consist of a host matrix with low phonon energy and active (dopant) ions. The selection of an appropriate host matrix plays a crucial role in the production of phosphors tailored for specific applications. Perovskites, both inorganic and organic, are currently being utilized as host matrices in the synthesis of nanophosphors. Perovskites are categorized into two subgroups: A²⁺B⁴⁺(O²⁻)₃ and A³⁺B³⁺(O²⁻)₃ based on their cationic states [1]. The first subgroup, where A represents large divalent metal ions and B represents tetravalent metal ions, are the

subgroup to which SrZrO₃ is a member. The 4d0 band ceramic SrZrO₃ perovskite has garnered significant attention as a material with novel technological applications due to its thermal/chemical stability [2–4], and substantial optical transparency. The slightly low vibrational frequency of SrZrO₃ makes it suitable as a host matrix for downshifting phosphors [5–7].

Research has indicated that modifying the properties of the host material, including its electronic structure and rare-earth ion concentration, can significantly influence its optical properties [8,9]. In this study, SrZrO₃ perovskite nanophosphors were modified through the addition of Na at the A site, resulting in the formation of NaSrZrO₃. This modification aimed to achieve low phonon energy and enhance strong emission intensity when doped with rare-earth ions such as Er³⁺. It is noteworthy that, despite extensive studies on the downshifting (DS) emission properties of rare-earth ion-doped SrZrO₃ under UV photoexcitation [10–12], there is currently no available information on the downshifting emission behavior of Er³⁺ in NaSrZrO₃ perovskite-based nanophosphors.

In this study, we effectively synthesized NaSrZrO₃:Er³⁺ with a

* Corresponding author.

E-mail address: armando.reyes@cimav.edu.mx (A. Reyes-Rojas).

<https://doi.org/10.1016/j.jalcom.2024.174104>

Received 24 November 2023; Received in revised form 16 February 2024; Accepted 6 March 2024

Available online 8 March 2024

0925-8388/© 2024 Elsevier B.V. All rights reserved.

pristine structure using the sol-gel reaction method. The doped samples displayed green emission, contrasting with the blue emission from the host material with high color purity and tunable by varying the concentration of Er^{3+} . Comprehensive investigations were conducted on the structural and optical properties, as well as the luminescent mechanism. The primary objective was to differentiate among various crystal phases of the host material and to explore potential applications of these phosphors in solid-state lighting for compact fluorescent lamps and LED lamps.

2. Experimental

2.1. Chemicals

Strontium Nitrate Anhydrous ($\text{Sr}(\text{NO}_3)_2$, 99.70%), Sodium nitrate (NaNO_3 , 99.99%), Erbium(III) nitrate pentahydrate ($\text{ErH}_{10}\text{N}_3\text{O}_{14}$), Zirconium (IV) 2,4-pentanedionate ($\text{C}_{20}\text{H}_{28}\text{ZrO}_8$, 99.72%), citric acid ($\text{C}_6\text{H}_8\text{O}_7$, 99.5%), and ethylene glycol ($\text{C}_2\text{H}_6\text{O}_2$, $\geq 99\%$). All chemicals are of analytical grade and were used without further purification.

2.2. Synthesis of $\text{NaSrZrO}_3:\text{Er}^{3+}$ phosphors

The citrate-ethylene glycol sol-gel reaction techniques was utilized to prepare $\text{Na}_{0.2}\text{Sr}_{0.9-x}\text{ZrO}_3:\text{Er}_x$ ($x = 0, 0.01, 0.02, 0.03, 0.04$ and 0.05) in accordance with our previous report [7]. Stoichiometric amount of starting material $\text{Sr}(\text{NO}_3)_2$, NaNO_3 , $\text{C}_{20}\text{H}_{28}\text{ZrO}_8$, $\text{ErH}_{10}\text{N}_3\text{O}_{14}$, $\text{C}_6\text{H}_8\text{O}_7$ and $\text{C}_2\text{H}_6\text{O}_2$ were weighed and mixed in 60 ml deionized water under vigorous stirring at $\sim 80^\circ\text{C}$ for 5 hours to form the xerogel. The xerogel was crushed into fine powder and preheated at 400°C in a muffle furnace for 2 h under air atmosphere with $5^\circ\text{C}/\text{min}$ heating rate. The powder sample was further annealed at 1050°C for 4 hours to obtain $\text{Na}_{0.2}\text{Sr}_{0.9-x}\text{ZrO}_3$ nanophosphors (abbreviated as NaSrZrO_3). Afterward, the sample was grinded again and collected for characterization. The samples were designated based on Er-doping concentrations, namely Er-0 for undoped (or $x = 0$), Er-1 ($x = 0.01$), Er-2 ($x = 0.02$), Er-3 ($x = 0.03$), Er-4 ($x = 0.04$), and Er-5 ($x = 0.05$).

2.3. Characterization

The samples were analyzed using various techniques: X-ray diffraction (XRD) patterns of samples in 2θ angular range from 10° to 80° were obtained using a Bruker D8 Discover diffractometer with CuK ($\lambda = 0.15418 \text{ \AA}$) radiation and a 1D detector Lynxeye in diverging beam geometry. Raman spectra were obtained using an XploRA INV-Horiba inverted Raman microscope, with a 532 nm laser and 50 mW power, in the $90\text{--}1200 \text{ cm}^{-1}$ range. The diffuse reflectance was measured using a Shimadzu UV-1280 UV-VIS-NIR scanning spectrophotometer in the range 190 and 1100 nm . Scanning electron microscopy (SEM) and energy dispersive X-ray spectroscopy (EDS) were performed on a Hitachi SU3500 SEM. Fourier transforms infrared (FTIR) spectroscopy was conducted on an AIM-9000 FTIR Spectrometer in the wave number region 400 cm^{-1} to 4000 cm^{-1} . Photoluminescence experiments was performed using a Hitachi F-7000 fluorescence spectrophotometer. PL spectra were recorded at room temperature using a PMT detector while the samples were excited by, He-Cd laser of wavelength of 325 nm .

3. Results and discussion

3.1. XRD analysis of $\text{NaSrZrO}_3:\text{Er}^{3+}$ phosphors

The XRD pattern of $\text{NaSrZrO}_3:\text{Er}^{3+}$ phosphors, as depicted in Fig. 1 (a), is indexed to the orthorhombic structure (space group Pnma , no. 62) of bulk SrZrO_3 , in accordance with the JCPDS card no. 004-0161. The presence of a monoclinic ZrO_2 phase, indicated by the circle symbol, was observed only in the undoped sample (JCPDS 078-0047). All the peaks in the XRD patterns of the prepared phosphors confirm the successful

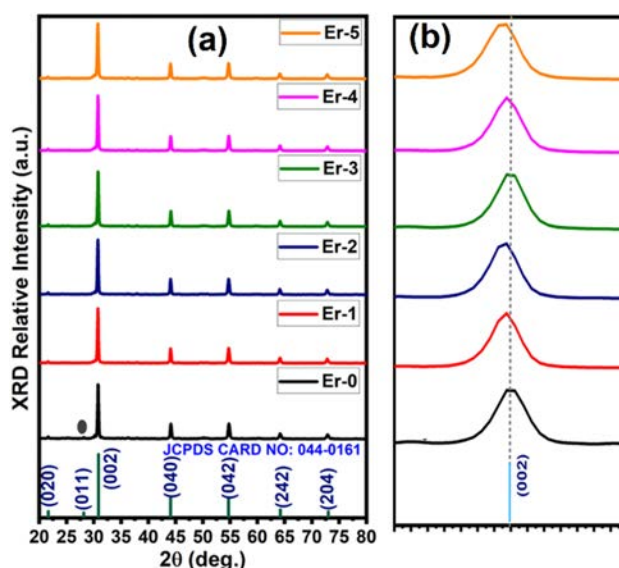


Fig. 1. (a) XRD patterns and (b) XRD peak shift at $2\theta^\circ = 30.85$ for $\text{NaSrZrO}_3:\text{Er}^{3+}$ phosphors.

substitution of rare earth elements at the host lattice sites. The coordination number of Sr^{2+} and Na^+ in NaSrZrO_3 is 12 (cuboctahedra). On the other hand, Zr^{4+} exhibits a coordination number of 6 with its neighboring oxygen atoms in the octahedron [13]. The difference in ionic radii between Er^{3+} and Zr^{4+} is large [14] so, the displacement of Zr^{2+} by Er^{3+} in the octahedron is expected to cause a significant distortion of the crystal structure, leading to a large peak shift to higher angle. However, no substantial peak shift was observed and moreover, the (002) peak shift was towards lower angles in all Er-doped NaSrZrO_3 samples (as shown in Fig. 1b) indicating a rather substitution of Er^{3+} at Sr/Na site and the presence of distortion in the crystal lattice of the host. The tolerance factor, t which determine the degree of disorder or stability in a perovskite was determined on the $\text{Na}_{0.2}\text{Sr}_{0.9-x}\text{ZrO}_3:\text{Er}_x$ ($x = 0, 0.01, 0.02, 0.03, 0.04$ and 0.05 mol\%) using the expression [15,16]:

$$t = \frac{(x_{\text{Na}} \times R_{\text{Na}}) + (x_{\text{Sr}} \times R_{\text{Sr}}) + (x_{\text{Er}} \times R_{\text{Er}}) + R_{\text{O}}}{\sqrt{2}((x_{\text{Zr}} \times R_{\text{Zr}}) + R_{\text{O}})} \quad (1)$$

where x is the mol fractions (mol ratios) of the constituent ions, R_{Na} , R_{Sr} , R_{Er} , R_{Zr} are ionic radii of the metal ions and R_{O} is ionic radius of the anion (oxygen ion) in their coordination numbers in the $\text{NaSrZrO}_3:\text{Er}^{3+}$ perovskite phosphors. the values of ionic radii were taken from Jia (1991) [14]. The calculated tolerance factor range between 0.99 and 0.85 for $x = 0$ to $x = 0.05 \text{ mol fraction}$. The reduction in the tolerance factor below 0.90 is a confirmation of phase transformation from predominantly cubic to orthorhombic phase of SrZrO_3 perovskite.

Utilizing the Scherrer formula, the crystal sizes (D) of the nanophosphors were estimated based on data extracted from the XRD pattern [17,18]:

$$D = \frac{0.89\lambda}{\beta \cos \theta} \quad (2)$$

where $\lambda = 1.5418 \text{ \AA}$, θ is the Bragg angle, and β is the FWHM of the diffraction peak [19]. The estimated crystallite sizes revealed a significant dependence on the concentration of Er^{3+} as depicted in Table I.

3.2. Optical properties of $\text{NaSrZrO}_3:\text{Er}^{3+}$ phosphors

The impact of Er^{3+} concentration on the optical properties of NaSrZrO_3 nanocrystals is evident from the measurement results of the ultraviolet-visible (UV-vis) diffuse reflectance spectra, as illustrated in

Table I

Evolutions of the crystallite sizes and optical band gaps of Er^{3+} -doped NaSrZrO_3 nanoparticles.

Sample Identity	FWHM (002)	Crystallite size (nm)	Optical band gap (eV)
Er-0	0.2377	36.21(4)	5.19
Er-1	0.2225	38.68(4)	5.30
Er-2	0.2232	38.56(4)	5.36
Er-3	0.2277	37.80(4)	5.24
Er-4	0.2276	37.82(4)	5.27
Er-5	0.2506	34.34(4)	5.22

The number between parentheses represents the error in the last number

Fig. 2 (A). The spectra reveal eight distinct absorption peaks at 214, 286, 380, 489, 523, 658, 979, and 1088 nm. It is noteworthy that two absorptions at 214 and 286 nm are attributed to the intrinsic absorption of the host. The spectral bands at 380, 489, 523, 658, and 979 nm correspond to observed absorption lines resulting from intraconfiguration f-f transitions. These transitions occur from the lowest levels of the $^4\text{I}_{15/2}$ ground state of erbium to the levels of the excited $^4\text{G}_{11/2}$, $^4\text{F}_{7/2}$, $^2\text{H}_{11/2}$, $^4\text{F}_{9/2}$, and $^4\text{I}_{13/2}$ states of the Er^{3+} ion. Notably, in Er^{3+} -doped samples, the intrinsic absorption peak shifted to 220 nm with an increase in dopant concentration.

The energy bandgap of the synthesized samples was determined using a combination of the Kubelka-Munk (K-M) model with Tauc's-Wood relation. The Kubelka-Munk theoretical model utilizes the K-M scattering and absorption coefficients, denoted as S and A, respectively, to describe the fraction of scattered and absorbed light per unit vertical length. This model is particularly effective when the particle size is comparable to or smaller than the wavelength of the incident light. It allows for the combination of reflection, refraction, and diffraction effects into a single scattering effect. Additionally, the reflectance value (R) remains unaffected by the thickness of the sample or sample holder in an infinitely thick sample. The K-M equation is depicted in Eq. 3 [20–22]:

$$\frac{A}{S} = \frac{(1 - R_\infty)^2}{2R_\infty} = F(R_\infty) \quad (3)$$

where, $F(R_\infty)$ is called Kubelka-Munk function or remission equivalent to the absorption coefficient, α . The band gap (E_g) and absorption coefficient (α) for parabolic band structure of an indirect band gap semiconductor are related through Tauc's-Wood relation [23,24]:

$$\alpha h\nu = K(h\nu - E_g)^n \quad (4)$$

where α is the linear absorption coefficient of the material, $h\nu$ is the photon energy and K is a proportionality constant. Combining the

remission function in Eq. (3) with the Tauc's-Wood relation in Eq. 4, gives the expression:

$$[F(R_\infty)h\nu]^n = K(h\nu - E_g) \quad (5)$$

For semiconductor materials with indirect band gaps, n equals 2 [7, 25,26]. Plotting $[F(R_\infty)h\nu]^2$ against $h\nu$ as shown in Fig. 2B, the band gap E_g of the samples were extrapolated from the linear fit of the straight-line portion of the curve, extrapolated to the $h\nu$ -axis with $[F(R_\infty)h\nu]^2 = 0$.

In Fig. 2B, the optical band gaps of Er^{3+} doped NaSrZrO_3 phosphors exhibit an increase value from 5.17 eV to 5.36 eV as the concentration of Erbium increases from 0 to 0.02. However, with further increases in concentration from 0.02 to 0.03, the optical bandgap energy decreases from 5.36 eV to 5.24 eV. There is a slight increase in the bandgap from 5.24 eV to 5.27 eV at 0.04 Erbium concentration, followed by a further decrease to 5.22 eV at 0.05 concentrations of the dopant.

It is worth noting that the experimental optical bandgap values for pure SrZrO_3 are somewhat uncertain, ranging from 5.0 eV to 5.7 eV, depending on the preparation process reported by other researchers [27–29]. The changes in the optical band gaps with Er^{3+} concentrations are illustrated in Table I. The observed blue shift in the absorption edge of the band from 0 to 0.02 Erbium content can be attributed to changes in lattice constants due to surface/interface states beyond the quantum confinement resulting from the small crystal size. In the case of high doping or a high carrier concentration ($\text{Er}^{3+} \leq 0.05$) in NaSrZrO_3 nanophosphor, there is a narrowing of the band gap, leading to a red shift.

3.3. Morphological studies of Er^{3+} -doped NaSrZrO_3 phosphors

The surface morphology of the synthesized $\text{NaSrZrO}_3:\text{Er}^{3+}$ phosphors examined by Scanning electron microscopy (SEM) is illustrated in Figs. 3(a) to 3(f). The SEM images depict a combination of large and small nearly spherical particles, with some forming agglomerations. Er^{3+} -doped samples exhibit more dispersed particles agglomeration. The images also reveal the presence of voids and pores, likely attributed to the release of significant gas amounts during sintering.

The EDX data [Fig. 3(g) – (i)], demonstrate an atomic ratio close to the theoretical value of pure $\text{NaSrZrO}_3:\text{Er}^{3+}$ concentration (refer to Table II). Major peaks in emission energies for Sr, Na, O, Zr, and Er were observed at 1.806 (La), 1.040 (Ka), 0.523 (Ka), 2.042 (La), and 6.947 (La) keV, respectively, in the sample. No impure elements were detected.

To further enhance comprehension, we investigated the structure and shape of the nanoparticles using high-resolution transmission electron microscopy (HRTEM). Fig. 4 presents images captured at the same magnifications for both the Er-0 sample and the Er-3 sample. The

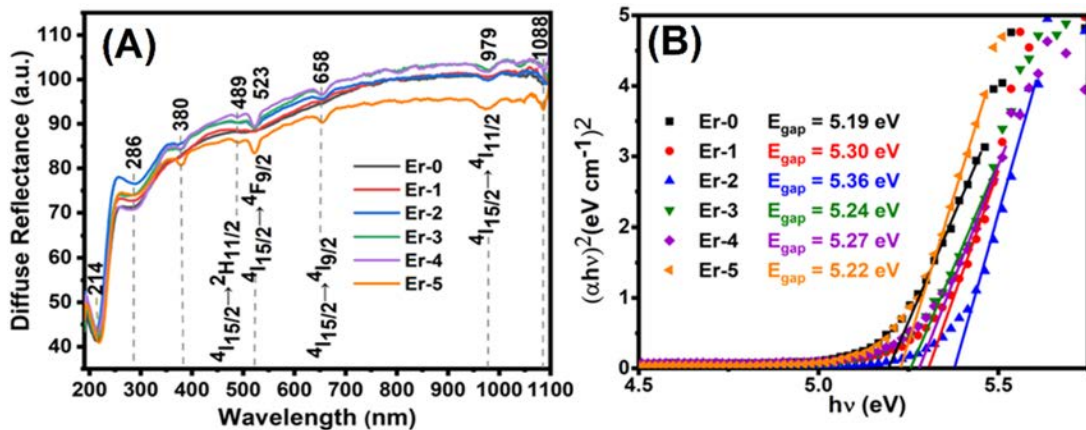


Fig. 2. Diffuse Reflectance spectra: (A) and Band gap energies (B) $\text{NaSrZrO}_3:\text{Er}^{3+}$ phosphors.

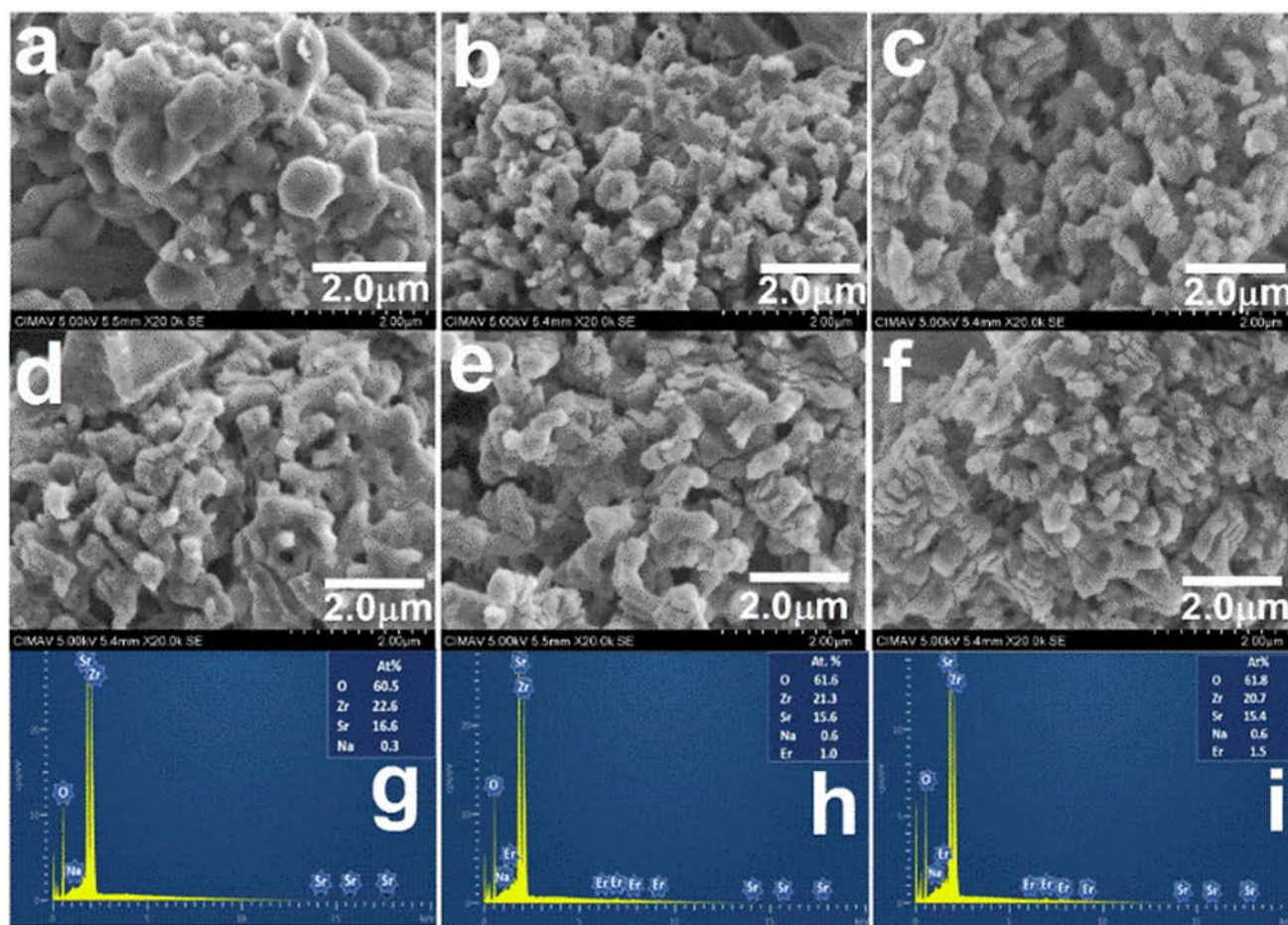


Fig. 3. Typical SEM images of (a) Er-0, (b) Er-1, (c) Er-2, (d) Er-3, (e) Er-4, (f) Er-5, and EDX of (g) Er-0, (h) Er-3, (i) Er-5.

Table II

Elemental composition of NaSrZrO₃:Er³⁺ phosphors determined by EDXA-SEM analysis.

Elements	at% Er-0	at% Er-1	at% Er-2	at% Er-3	at% Er-4	at% Er-5
O	60.5	65.5	62.3	61.6	61.6	61.8
Zr	22.6	17.8	20.3	21.3	19.8	20.7
Sr	16.6	16.2	16.6	15.6	17.3	15.4
Na	0.3	0.3	0.4	0.6	0.3	0.6
Er	***	0.2	0.4	1.0	1.0	1.5

observations from Figs. 4a and 4b indicate that the undoped nanoparticles exhibit an almost cube-shaped morphology, whereas the doped counterparts display a nearly spherical shape. This suggests a modification in the structure of the host matrix induced by the dopant. The average particle sizes for pure and erbium-doped nanoparticles are 24 nm and 33 nm, respectively. The increase in erbium concentration is evident in both particles determined from TEM and crystallite sizes obtained from XRD calculations.

Nevertheless, the TEM images reveal a higher propensity for agglomeration in comparison to the pure nanoparticles. The analysis unveiled distinct grain morphologies in all samples, with a uniform grain diameter measuring approximately 5 nm. A comprehensive examination of these grains was conducted using HRTEM images. The images disclose that the interplanar distances of the nanocrystallites in both pure and doped samples measure 3.61 Å and 3.67 Å, respectively (Figs. 4c and 4d), corresponding to the (111) lattice plane of the

orthorhombic SrZrO₃ perovskite (JCPDS 44–0161). Elemental mapping in Fig. 4(e–i) illustrates the uniform distribution of Sr, Na, Er, O, and Zr over the specified region.

3.4. Specific surface area analysis of NaSrZrO₃:Er³⁺ phosphors

Nanomaterials exhibit distinctive properties attributed to their high surface-to-volume ratio; a characteristic that intensifies as the particle size decreases. In contrast to bulk materials, wherein the majority of atoms reside in the interior, nanomaterials are predominantly composed of surface atoms. This dominance at the surface amplifies reactions occurring, including dissolution, oxidation, and photo-excitation. The Brunauer-Emmett-Teller (BET) surface adsorption method is frequently employed to quantitatively assess the surface area of nanomaterials.

Fig. 5 illustrates the nitrogen adsorption-desorption isotherms and pore size distribution curves. Both the pure NaSrZrO₃ sample and those doped with Er³⁺ exhibit a type II isotherm, consistent with IUPAC categorization [30,31]. Table III presents specific surface area (S_{BET}), total pore volume (V_{total}), and average pore diameter (D_p) for all synthesized samples. According to the table, the synthesized NaSrZrO₃:Er³⁺ nanocrystals exhibit specific surface areas ranging from 3.526 to 6.403 m²g⁻¹, average pore diameters ranging from 18.396 to 36.7 nm, and average pore volumes ranging from 0.016 to 0.052 cm³g⁻¹. Contrary to the general rule that surface area decreases with increasing volume, there are situations where both parameters increase, as in this case. The explanation lies in the fact that as the pore volume increases, the number of pores accommodating nitrogen also increases, ultimately

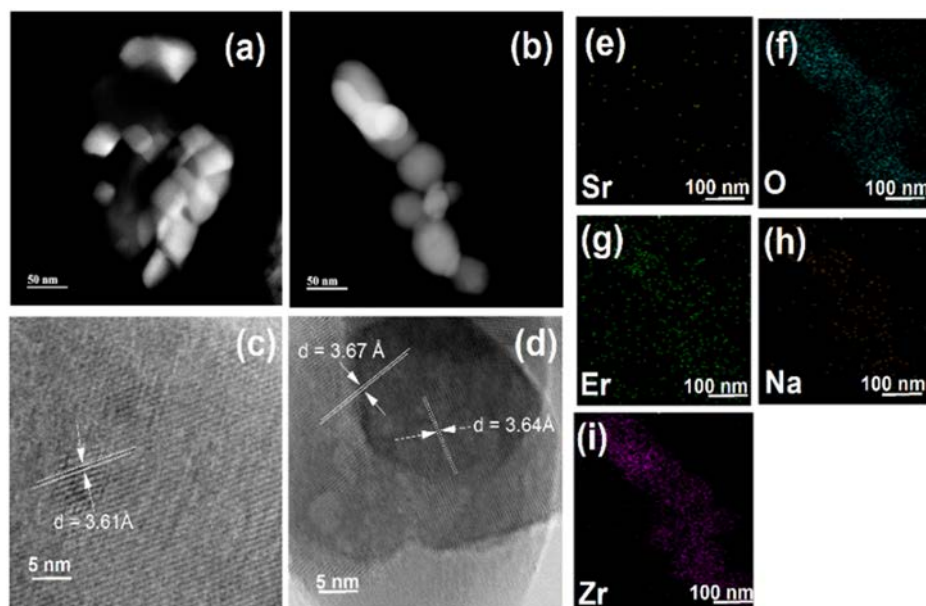


Fig. 4. (a,b) HRTEM images, (c,d) lattice fringes from HRTEM analysis of Er-0 and Er-3 respectively; (e-i) elemental mapping of Er-3 of $\text{NaSrZrO}_3:\text{Er}^{3+}$ phosphors.

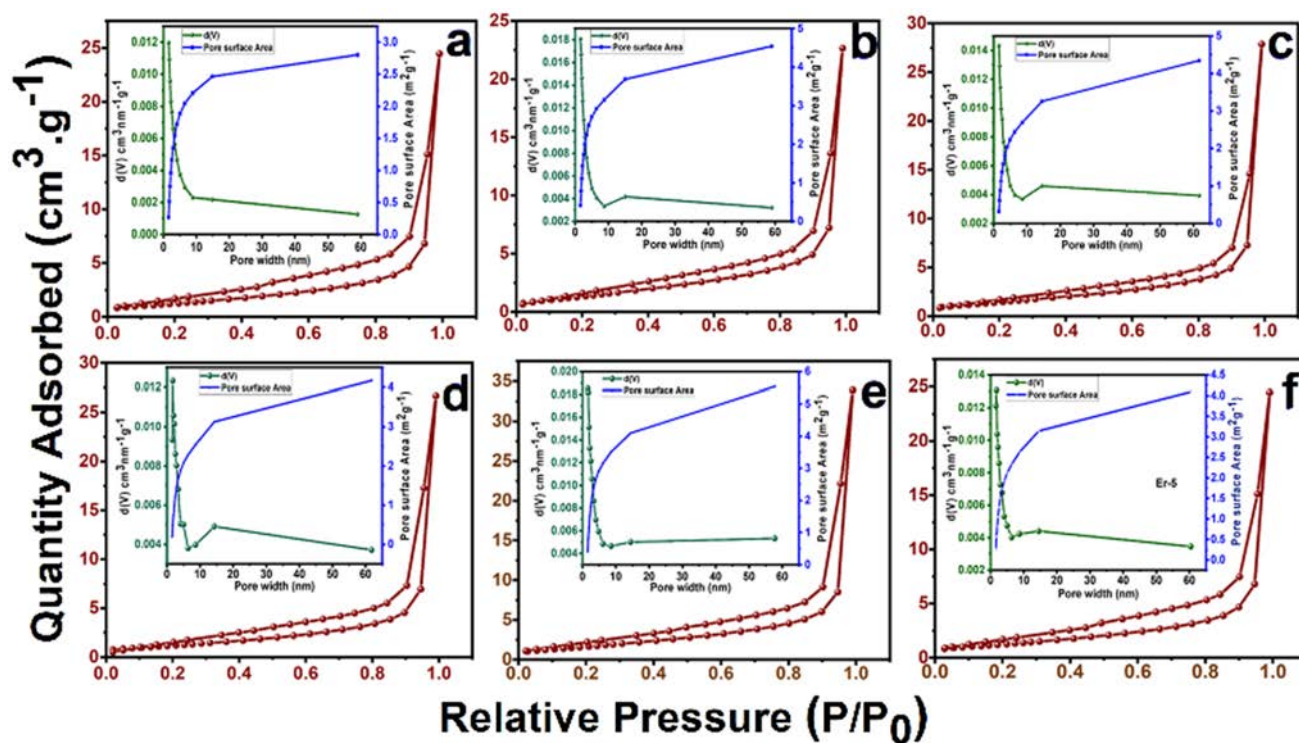


Fig. 5. The nitrogen adsorption-desorption isotherms and corresponding pore size distribution curves of pure (a) Er-0 (b) Er-1 (c) Er-2 (d) Er-3 (e) Er-4, and (f) Er-5.

resulting in an increase in surface area [32–34].

3.5. Micro-Raman analysis of $\text{NaSrZrO}_3:\text{Er}^{3+}$ phosphors

Raman spectroscopy is a widely employed technique for investigating the correlation between lattice vibrational modes and resonant patterns. In Fig. 6(a), the Raman spectrum of $\text{NaSrZrO}_3:\text{Er}^{3+}$ nanocrystals are depicted within the range of 100 cm^{-1} to 1200 cm^{-1} . The identified peaks are based on the analogous compounds of SrZrO_3 .

The factor group analysis reveals that the irreducible representation Γ of the phonon modes at the zone center can be deconstructed into the following components: $\Gamma = 7A_g + 5B_{1g} + 7B_{2g} + 5B_{3g} + 8A_u + 10B_{1u} + 8B_{2u} + 10B_{3u}$. Among the 24 modes, $7A_g$, $5B_{1g}$, $7B_{2g}$, and $5B_{3g}$ are Raman active, whereas B_{1u} , B_{2u} , and B_{3u} account for the three acoustic modes. Additionally, the 25 infrared active modes consist of $9B_{1u}$, $7B_{2u}$, and $9B_{3u}$, while the $8A_u$ modes remain silent.

In the Raman spectroscopic examination of ABO_3 perovskite crystals, spectral features are distinguished as either oxygen octahedral internal

Table III
Textural parameters of NaSrZrO₃:Er³⁺ phosphors.

Sample ID:	S _{BET} (m ² g ⁻¹)	BHJ (nm)		Average Pore Diameter (D _p) (nm)	Pore Volume (V _{total}) (cm ³ g ⁻¹) at P/P ₀ = 0.099
		Adsorption	Desorption		
Er-0	3.526	1.563	1.712	18	0.016
Er-1	5.324	1.571	1.533	26	0.035
Er-2	5.444	1.563	1.922	32	0.041
Er-3	4.498	1.753	1.908	37	0.043
Er-4	6.403	1.554	1.897	33	0.052
Er-5	4.707	1.750	1.885	32	0.037

or external modes. This distinction arises from lattice vibrations, commonly known as soft modes, which respond to the movement of cations within the oxygen octahedral framework. In Fig. 6(a), the Raman frequency range of 100 cm⁻¹ to 200 cm⁻¹ is assigned to lattice vibrations associated with the Sr²⁺ ion in the A-site within the ZrO₆ octahedron. The primary contributor to this vibration is the lowest frequency vibrator, labeled as "a = Sr-ZrO₃ torsional zone," centered at A_g (157 cm⁻¹). This specific vibration is responsible for the observed spectral features in this frequency range.

Tarrida and colleagues [35] found that the low-energy Raman bands in (Ca, Sr)ZrO₃ and Ca(Sn, Zr)O₃ perovskite compounds are affected by the mass of the A cation and the shift to lower energies. It was also found that the deficiency of Sr (V_{sr}[']) in SrZrO₃ increases the occurrence of oxygen vacancies (V_o[']) [36–38].



Vibrators 'b' and 'c' (within the range of 200 cm⁻¹ to 600 cm⁻¹) are generated by the bending and stretching of the ZrO₆ octahedron, primarily associated with O₂[']. Vibrator 'd' (spanning from 600 to 900 cm⁻¹) is related to defect stretching vibrations of Zr-O. In Fig. 6(b), a broad spectral feature is observed at frequencies above 900 cm⁻¹ (vibrator 'e') for all Er doped samples. This feature cannot be attributed to the symmetry-related stretching vibration of strontium zirconate [39]. Neutron inelastic scattering studies of the lattice dynamics of strontium titanate suggest that the observed high frequency feature can be interpreted as a two-phonon scattering [40,41]. It has been concluded

that the intra-ionic polarizability of oxygen in Sr-O planes governs the second order Raman spectra in Sr-containing perovskite oxides. The undoped spectrum displays a distinct narrow band around ~36 cm⁻¹, while the doped samples exhibit strong and broad bands around ~460 cm⁻¹ and ~740 cm⁻¹, which are typical of monoclinic zirconia [42,43]. Despite this, the XRD analysis indicates the existence of only a minor ZrO₂ phase in the pure sample lacking Erbium ions. It can be inferred that surface stress effects cause monoclinic deformation of ZrO₆ octahedra at the outer surfaces and bulk grain boundaries.

To discern Raman normal modes, the Raman shifts and FWHM are two crucial parameters. A Gaussian fitting function, employed as a deconvolution function, was used to fit the parameters of the phonon modes for the samples (refer to Fig. 6b), and Table IV presents a comprehensive list of all phonon modes along with their symmetries. The comparison between pure and Er-doped samples was conducted, revealing similar trends with slight differences in peak positions detailed in Table IV. Despite a marked increase in overall peak intensity for the doped samples, the majority of Raman modes still manifested in the Er-doped sample, albeit with a slight shift in peak position.

In all samples, the bands at 157 cm⁻¹ represented first-order Raman modes associated with specific lattice distortions and defects in the host matrix. Prior research has proposed that disorder on the B sublattices in the ABO₃ perovskite contributes to the appearance of first-order Raman scattering features [44]. Consequently, it is anticipated that the degree of ordering on the B-site is higher in the Er-doped sample, consistent with previous reports for Sn, La-perovskite compared to Zr perovskite [45–47]. The weak shoulders identified in pure NaSrZrO₃ became more pronounced upon Er incorporation, especially beyond 750 cm⁻¹, attributed to an increase in elastic scattering sources for both phonon and electron systems. It is evident that the substitution of Er for Sr cations led to the augmentation of certain Raman modes. This shift in lattice dynamics is a consequence of the partial substitution of Er³⁺ for Sr²⁺.

3.6. Photoluminescence analysis of NaSrZrO₃:Er³⁺

The downshifted (DS) photoluminescence spectra of NaSrZrO₃:Er³⁺ phosphors recorded in the fluorescent mode between 350 and 700 nm under 325 nm excitation are depicted in Fig. 7(a). The undoped

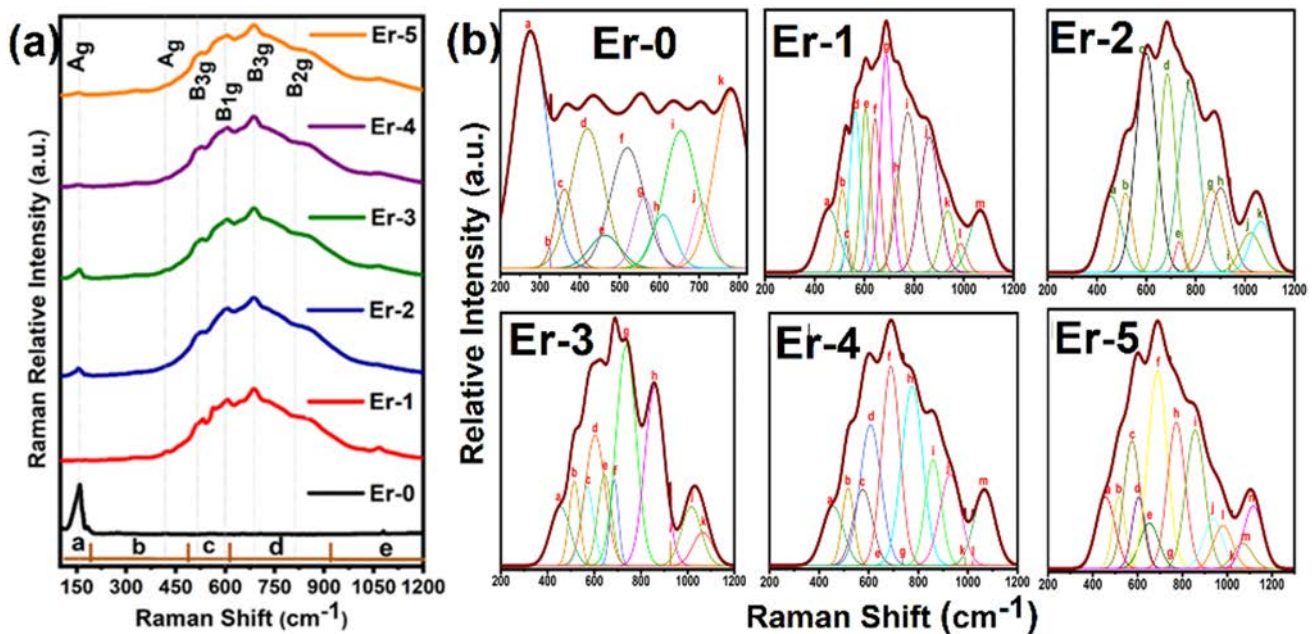


Fig. 6. (a). Raman spectra for pure and Er-doped, (b). Deconvolution of Raman spectra for NaSrZrO₃:Er³⁺ phosphors.

Table IV

Raman peak position (cm^{-1}), FWHM and symmetry assignment.

Er-0 Peak Index	Positions (cm^{-1})	FWHM	Raman Symmetry	Er-1 Peak Index	Positions (cm^{-1})	FWHM	Raman Symmetry	Er-2 Peak Index	Positions (cm^{-1})	FWHM	Raman Symmetry
a	275	100	A_g	a	457	100	B_{2g}	a	459	100	B_{2g}
b	327	0.0946	B_{1g}	b	512	45.6430	B_{3g}	b	517	63.5993	B_{3g}
c	361	55.8230	B_{2g}	c	528	21.1404	B_{3g} or B_{1g}	c	601	100	A_g
d	419	97.4475	A_g	d	564	51.2799	B_{1g}	d	687	76.1589	B_{3g}
e	464	90.9428	B_{2g}	e	606	45.1546	A_g	e	734	40.3494	B_{3g}
f	519	100	B_{3g}	f	644	46.6978		f	774	100	B_{1g}
g	562	61.2316	B_{1g}	g	688	52.8295	B_{3g}	g	866	100	
h	610	70.3242	A_g	h	733	48.1315		h	903	100	
i	654	100	B_{3g}	i	777	90.0795	B_{3g}	i	938	0.1208	
j	708	56.9643		j	863	91.9013	B_{1g}	j	1024	100	
k	781	100	B_{1g}	k	937	67.8986		k	1065	100	
				l	988	56.6722					
				m	1067	100					
Er-3 Peak Index	Positions (cm^{-1})	FWHM	Raman Symmetry	Er-4 Peak Index	Positions (cm^{-1})	FWHM	Raman Symmetry	Er-5 Peak Index	Positions (cm^{-1})	FWHM	Raman Symmetry
a	456	100	B_{2g}	a	454	100	B_{2g}	a	455	100	B_{2g}
b	516	53.6818	B_{3g}	b	515	56.1045	B_{3g}	b	515	65.5155	B_{3g}
c	570	65.9011	B_{1g}	c	574	91.1543	B_{1g}	c	573	87.1935	B_{1g}
d	605	100	A_g	d	605	100	A_g	d	603	69.4371	A_g
e	646	68.6794	B_{3g}	e	646	0.0251	B_{3g}	e	650	99.5129	B_{3g}
f	687	42.0336		f	687	85.7357		f	687	100	
g	738	100	B_{2g}	g	736	0.0594	B_{2g}	g	741	0.2154	B_{2g}
h	860	100		h	773	100	B_{1g}	h	771	93.6858	B_{1g}
i	927	0.0080		i	857	76.8475		i	856	100	
j	1017	100		j	927	100		j	935	100	
k	1066	100		k	986	0.0086		k	979	100	
				l	1018	0.0224		l	1017	0.0481	
				m	1065	100		m	1067	100	
								n	1114	100	

NaSrZrO_3 sample (Er-0) has a broad band in the range 350–750 nm. The deconvolution of this spectrum using Gaussian fitting gave seven bands at about; 378, 430, 460, 496, 560, 604, and 703 nm which have been associated with structural disorder in the SrZrO_3 host which present localized states in the band gap [48,49]. These bands which were analyzed comprehensively in our previous report are associated with both shallow and deep defect states formed by Zr–O and Sr–O complex clusters in the band gap of NaSrZrO_3 nanocrystals [7]. The Er^{3+} doped samples retained some of the host related emission bands, though blue-shifted, and also included the intraconfigurational transitions of Er^{3+} ion at about 523 and 546 nm corresponding to the $^2\text{H}_{11/2} \rightarrow ^4\text{I}_{15/2}$ and $^4\text{S}_{3/2} \rightarrow ^4\text{I}_{15/2}$, respectively. The stark splitting observed in the two green emission lines of erbium ions is attributed to the crystal field effect. Fig. 7(b) shows increasing trend of the 430, 523 and 546 nm emission intensities with increasing Er^{3+} concentration up to 3% and

thereafter their intensities declined at higher concentrations.

Similar to the fluorescent spectra in Fig. 7, we also recorded phosphorescence emissions of the same samples under 325 nm excitation by gating the detector to remain off until 0.3 ms after each excitation pulse and the results are presented in Fig. 8(a). The phosphorescence spectra showed four peaks with maxima at 430, 523, 546 and 703 nm. The broad peak at 430 nm and the split peak at 703 nm are reported to be due to localized defects in the host band gap as explained in the fluorescence case. However, there is the need to explain these bands in more details. In a SrZrO_3 -based perovskites, there are two forms of disorder; crystalline disorder and octahedra tilting disorder (which is dependent on the tolerance factor). The crystalline disorder is a function of crystallinity of the solid and is directly proportional to the diffraction peak intensity. The higher the crystallinity (peak intensity), the higher the degree of order in the crystal and vice versa. The diffraction peak

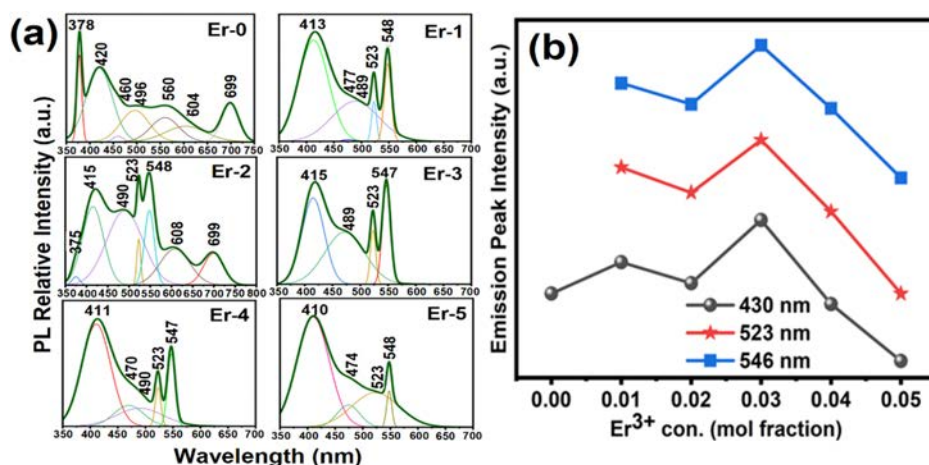


Fig. 7. a) Fluorescence emission spectra of $\text{NaSrZrO}_3:\text{Er}^{3+}$ phosphors under 325 nm excitation; b) Emission intensities at 430, 523 and 546 nm as a function of the Er^{3+} concentration.

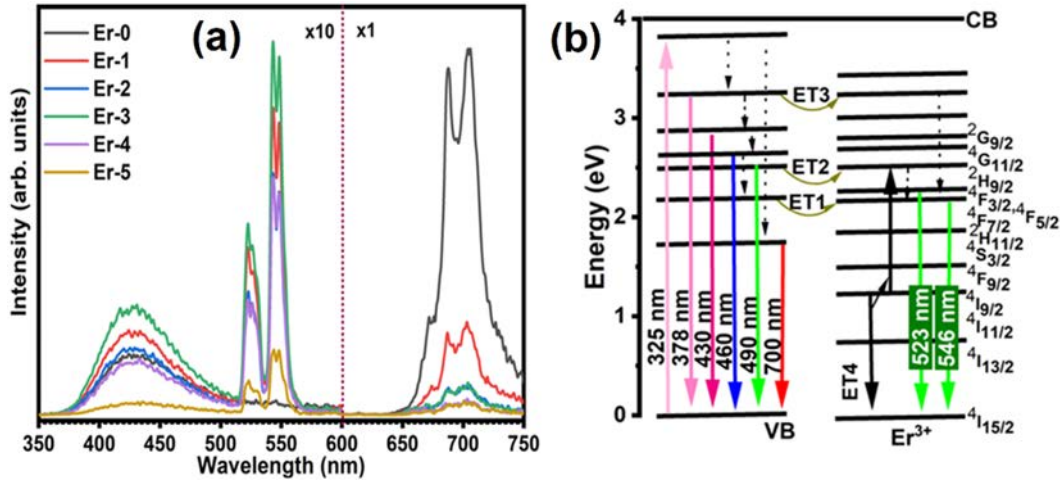


Fig. 8. (a) Photoluminescence emission spectra of NaSrZrO₃:Er³⁺ phosphors at 325 nm excitation. The region below 600 nm has been magnified 10x. (b) Energy level diagram.

intensity in Fig. 8(b) shows a linear increment with increasing Er³⁺ concentration demonstrating an increasing order in the crystal. The 430 nm emission band which has been deconvoluted into three bands (violet – blue bands) at about 378, 412, and 455 nm is known to depend on the crystalline disorder. The peak positions of these bands are found to change with increment of Er³⁺ ions. These violet-blue band were also identically reported by Lee et al. (2011) [49] to originate from structural disorder. While the violet-blue emission band have been extensively studied, the origin of the red emission peak at 703 nm is still been speculated. It is already confirmed that, this peak does not arise from impurities gotten in the process of synthesis nor is it coming from any rare-earth ion, but it is rather an inherent structural phenomenon in SrZrO₃ [48]. From Fig. 8(a), it can be seen that this emission peak (703 nm) is about 10-fold stronger than the intensities of other bands and decreases exponentially with increasing Er³⁺ concentrations as shown in Fig. 8(b). Curiously, also in Fig. 8(b), the tolerance factor is shown to decline in a similar manner as the 703 nm emission peak intensity with increasing Er³⁺ concentrations. Thus, the 703 nm emission peak intensity is dependent on the tolerance factor (stability) of the SrZrO₃-based perovskite; the higher the tolerance factor, the stronger is the 703 nm emission peak intensity and vice versa. The tolerance factor is known to moderate the distortion of the crystal by tilting the octahedra and ultimately changing the crystal symmetry. Therefore, the declining trend of the tolerance factor signifies a progressive distortion (octahedra tilting distortion) in the crystal structure of the host as a result of the increase substitution of smaller size Er³⁺ ions at the larger size Sr²⁺/Na⁺ sites in the host lattice, and the consequent lowering of the crystal symmetry. As already noted, only the 523 nm and 546 nm peaks are assigned to Er³⁺, and these lines showed increasing trend with increasing dopant ion concentration up to 3% concentration before the occurrence of luminescence quenching.

The observed luminescence quenching of the green emission lines (523 and 546 nm) could be associated with multiphonon relaxation or concentration quenching caused by energy transfer between Er³⁺ ions in the form of cross relaxation, migration, exchange interaction or multipolar - multipolar processes [50]. However, with the low phonon energy of the host (442 cm⁻¹), multiphonon processes are ruled out as possible cause of luminescence quenching in this material. The most likely quenching mechanisms for this material are therefore, exchange interaction or multipolar-multipolar processes. To ascertain which among these two processes account for the luminescence quenching, we first calculate the critical distance, R_c between the Er ions using the Blesse formula [51];

$$R_c = \left(\frac{3V}{4\pi xN} \right)^{1/3} \quad (7)$$

where V is the average unit cell volume, x is the critical concentration of Er³⁺ = 0.03 mol fraction and N is the number of ions in the unit cell. The calculate value of $R_c = 8 \text{ \AA}$ is larger than the 5 \AA (for exchange interaction), implying the quenching process is via the multipolar-multipolar interaction [52]. There are three possible multipolar processes; the dipole-dipole ($d-d$), dipole-quadrupole ($d-q$), and the quadrupole-quadrupole ($q-q$) interactions. The Van Uiter formula [50, 52,53] was used to determine which among these three multipolar processes is responsible for the luminescence quenching;

$$\frac{I}{x} = k(1 + \beta(x))^{-\theta/3} \quad (8)$$

where I is the quenching intensity, β and k are a constants, and θ with values as 6, 8, and 10 represent $d-d$, $d-q$, and $q-q$ multipolar processes, respectively. From the plots of $\log_{10}(I/x)$ versus $\log_{10}(x)$ in Fig. 9(a), the slopes of the linearly fitted section of the curves are -4.3 and -4.3 for 523 nm and 546 nm peaks, respectively of Er³⁺ ion, giving the value of $\theta = 12.9$ and 12.8 . These θ values are closer to the theoretical value of 10 suggesting the $q-q$ interaction is responsible for luminescence quenching in these samples.

Fig. 10 display the decay lifetime profiles of the undoped and all Er³⁺-doped samples for the 430, 523, 546, and 703 nm emission bands under the 325 nm excitation mode. All the samples gave multi-exponential decay profile defined by the function;

$$I(t) = \sum_{i=1,2,3} I_i \exp(-t/\tau_i) \quad (9)$$

The average lifetime was obtained using the expression;

$$\tau_i = \frac{\sum_{i=1,2,3} I_i \tau_i^2}{\sum_{i=1,2,3} I_i \tau_i} \quad (10)$$

where I_i is the lifetime intensity, t is the time after excitation and τ_i is the lifetime for the i^{th} component having intensity I_i . The decay curves for emissions at 523 nm, 546 nm and 703 nm were fitted with double exponential functions, while the longer decay curves for emission at 430 nm required three exponentials for a better fit.

Multi-exponential decay profile indicates the presence one or more of the following factors; different luminescent centres, nonradiative energy transfer processes, defects and the presence of impurities in the host [54]. Table V presents the average decay lifetimes of the different

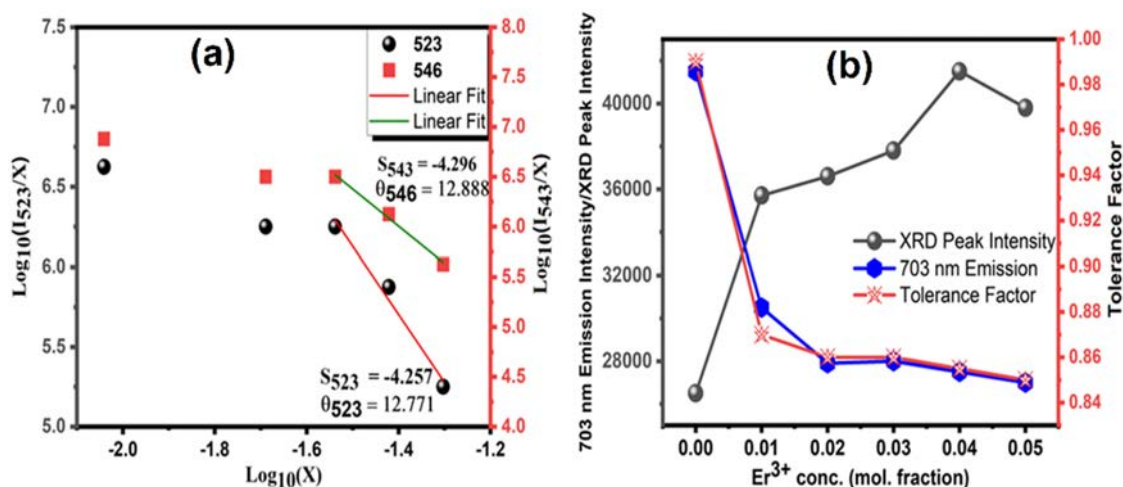


Fig. 9. (a) Plot of $\log_{10}(I/x)$ versus $\log_{10}(x)$, and (b) plots of tolerance factor, XRD peak peak intensity, and 703 nm emission intensity of $\text{NaSrZrO}_3: \text{Er}^{3+}$ phosphors.

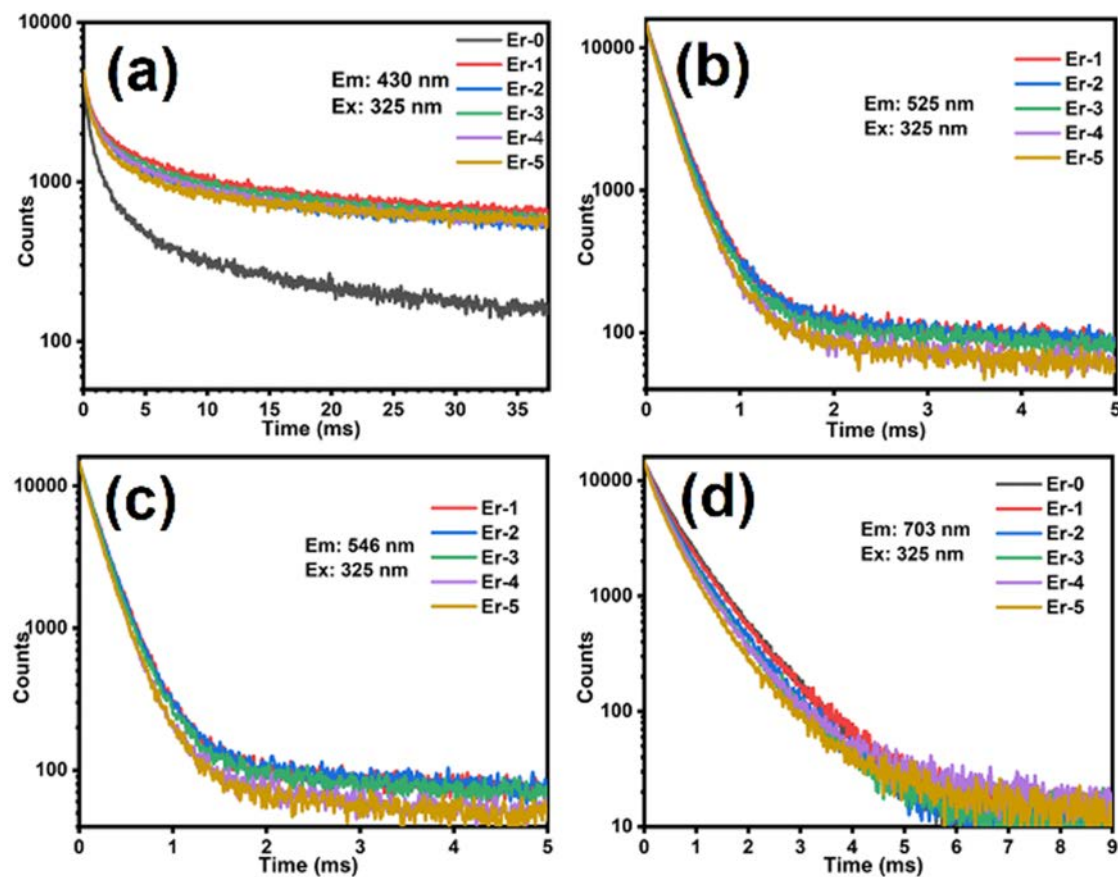


Fig. 10. Decay curves for emission peaks at (a) 430 nm, (b) 525 nm, (c) 546 nm, and (703 nm of $\text{NaSrZrO}_3: \text{Er}^{3+}$ phosphors.

emission band considered in this work. The average lifetime of the violet-blue emission band with peak maxima at 430 nm is the longest (~ 10 ms) and is likely persistent luminescence due to host crystal defects emanating from different pathways. Doping appeared to increase its lifetime albeit non-monotonically, due to generation of additional crystalline disorder (defects). On the other hand, decay lifetimes of the 523 and 546 nm (green) emissions are the shortest and similar, which is a sign of them emanating from about the same energy states. Moreover, the difference between the $^2\text{H}_{11/2}$ (523 nm) and $^4\text{S}_{3/2}$ (546 nm) states is

small, ≈ 0.09 eV (704 cm^{-1}). Also, the decay lifetimes of these $^4\text{S}_{3/2}$ and $^2\text{H}_{11/2}$ states are observed to decrease monotonically with increasing Er^{3+} ion concentration. This declining decay lifetime with increasing Er^{3+} ion concentration is attributed to self-quenching between neighbouring Er^{3+} ions. Self-quenching come about at higher Er^{3+} ion concentration because of enhanced non-radiative energy migration between Er^{3+} ions due to shortened distance between neighbouring Er^{3+} ions [55]. The decay lifetime of 703 nm (red) emission band is slightly longer than the decay lifetime of green emission lines, but far shorter than

Table V
Lifetimes (in ms) of emissions for NaSrZrO₃:Er³⁺ nanophosphors.

	525 nm	546 nm	703 nm	430 nm
Er-0	—	—	0.66 ms	8 ms
Er-1	0.30 ms	0.28 ms	0.65 ms	12 ms
Er-2	0.29 ms	0.29 ms	0.60 ms	9 ms
Er-3	0.27 ms	0.26 ms	0.57 ms	12 ms
Er-4	0.26 ms	0.24 ms	0.56 ms	10 ms
Er-5	0.24 ms	0.23 ms	0.53 ms	11 ms

lifetime for the violet-blue band. We also observed decreasing decay lifetime of the red emission band with increasing Er³⁺ ion concentration. This can be related to a progressive distortion of the perovskite structure by continuous tilting of the octahedra as more Er³⁺ ions displace Sr³⁺/Na⁺ in the host crystal lattice. Besides, the similarity in the average decay lifetime of the red emission band and the green emission bands shows that the localized defect states producing the former is also well defined.

It is important to note that in this case, the PL mechanism does not involve band-to-band transitions, as the excitation energy is significantly lower than the bandgap value obtained. The energy level diagram for the DS mechanism in Er³⁺-doped NaSrZrO₃ nanocrystals is depicted in Fig. 8(b). The process begins with the excitation of ions to energy state at 3.82 eV (325 nm) in the host band gap from where the ions relax nonradiatively to other defect levels. Some of these defect levels such as 378 nm (ET1), 490 nm (ET2) and 560 nm (ET3) overlap the ⁴G_{11/2}, ⁴F_{7/2}, and ⁴S_{3/2} energy levels of Er³⁺ (Fig. 8b) thus, transferring part (or all) of their energies to the dopant ions. This is evidence by the decrease intensity of these defect related bands with increasing Er³⁺ concentration and the eventual disappearance of some of the bands, especially the 560 nm band. The ions at upper lying ⁴G_{11/2}/⁴F_{7/2} levels relax non-radiatively to the ²H_{11/2}/⁴S_{3/2} levels followed by radiative relaxation to the ground level to produce the green emissions at 523/546 nm.

The quenching of luminescence from the ²H_{11/2} and ⁴S_{3/2} levels was already described to be a multipolar process which of course depends on the critical distance between neighbouring ions. At higher Er³⁺ ion doping (beyond 3 mol fraction), the ions tend to form clusters due to decreasing distance between them. The probability of energy transfer such as ET4 and cross-relaxation (CR) increases. For the ET4 process (Fig. 8b), two neighbouring Er³⁺ ions, both at excited ⁴I_{11/2} level interact, and with one of them acting as a donor, transfers its energy to a neighbouring Er³⁺ ion. The receiving ion gets excited to the ⁴F_{7/2} level from where it undergoes nonradiated relaxation to ²H_{11/2}/⁴S_{3/2} pairs giving out green emission. On the other hand, the donor ion relaxes

nonradiatively to the ground level after losing its energy. Similar to the ET4 process is the CR process where two Er³⁺ in close proximity are raised to an intermediate level (⁴I_{11/2}) and a CR process occurs by taking one of the ions to the ⁴F_{7/2} level, while the other ion returns non-radiatively to the ground level. Both of these processes are responsible for the decrease intensity of the green band at higher Er³⁺ concentrations. As can be seen in Fig. 8a, the red emission band at 700/703 nm is strictly emanating from the host and has no equivalent energy level in the Er³⁺ ion. Therefore, the quenching of the red emission band can be better explained as earlier discussed in this section.

3.7. CIE chromaticity coordinates

To determine the exact color emission and purity of the phosphor samples, we employed the chromaticity diagram from the International Commission on Illumination (CIE), based on the PL spectra obtained under 325 nm excitation (see Fig. 11a). The corresponding chromaticity coordinates are provided in Table VI. The pure sample emits blue light, while the doped sample emits green light (refer, Fig. 11 c), confirming that NaSrZrO₃:Er³⁺ nanocrystals can achieve different light colors when processed under the same preparation and excitation conditions. The correlated color temperature (CCT) [56], a parameter associated with color appearance, was calculated using the McCamy equation [57],

$$\text{CCT} = -449n^3 + 325n^2 - 6823.3n + 5520.33 \quad (11)$$

Where $n = (x - x_e)/(y - y_e)$ is the inverse slope of the line that is defined from the chromaticity epicentre given as $x_e = 0.3320$, $y_e = 0.1858$, where x and y are the sample chromaticity coordinates. CCT is measured in degrees Kelvin and spans a range from 1000 K to approximately 10,000 K. As the CCT increases, the light takes on a cooler or more bluish hue, whereas lower CCT values yield a warmer, more yellowish tone in the lighting.

In Table VI, the CCTs obtained for NaSrZrO₃:Er³⁺ range from 5794 K

Table VI
CIE coordinates, CCT and Color purity of NaSrZrO₃:Er³⁺ nanocrystals.

Samples	x	y	CCT (K)	Purity (%)
x = 0	0.146	0.045	1730.15	99.82
x = 0.01	0.284	0.678	6220.68	93.90
x = 0.02	0.314	0.649	5793.64	99.41
x = 0.03	0.283	0.682	6226.97	99.50
x = 0.04	0.280	0.683	6276.05	96.98
x = 0.05	0.291	0.667	6128.72	96.96

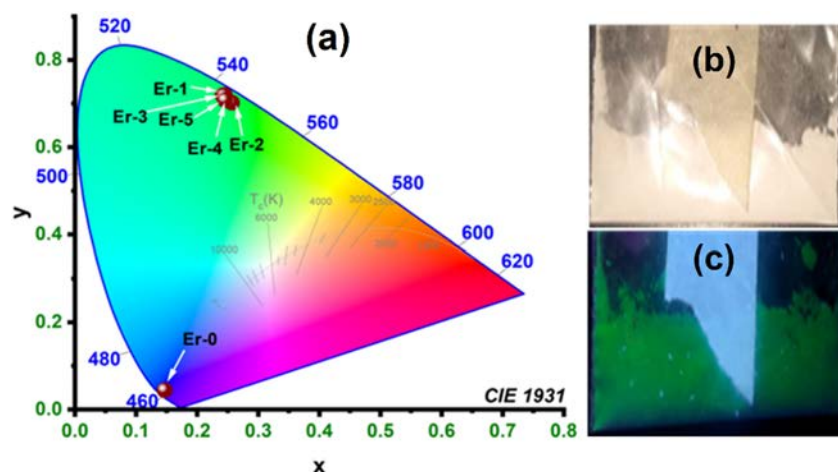


Fig. 11. (a) The CIE 1931 color coordinates of NaSrZrO₃:xEr³⁺ nanophosphors obtained using excitation at 325 nm. Phosphor powder image under (b) daylight, (c) 254 nm UV light.

to 6276 K for the doped samples. These values fall within the CCT range typical for cold white (natural light or Day white) compact fluorescent and LED lamps. This characteristic makes $\text{NaSrZrO}_3:\text{Er}^{3+}$ a suitable material for generating cool white light when combined with a blue-LED chip [58,59]. The sample without doping exhibited a lower CCT of 1730 K, signifying a warmer light temperature. These phosphors demonstrated exceptional color purity, exceeding 93%, across various correlated color temperatures and CIE coordinates, as detailed in Table VI. These results suggest that the prepared materials, NaSrZrO_3 and $\text{NaSrZrO}_3:\text{Er}^{3+}$, hold promise for applications as blue-emitting and green-emitting UV convertible phosphors, respectively.

4. Conclusion

Utilizing the sol-gel citrate-ethylene glycol route, we have successfully synthesized the orthorhombic phase of $\text{Na}_{0.2}\text{Sr}_{0.9-x}\text{ZrO}_3$ doped with Er^{3+} phosphors. A comprehensive investigation was conducted to analyze their structural, optical, and luminescent properties. The crystal structure was characterized through powder XRD measurements and supplemented by BET/pore size distribution analysis. The band gap analysis reveals that the optical band of the sample can be tuned (ranging between 5.19 and 5.36 eV) by adjusting the concentration of Er^{3+} ion values during synthesis. Under ~ 325 nm UV excitation, the developed nanophosphors exhibit robust emissions in the green and low red emission regions in the downshifting spectra. At low pump power density, the color tunability, as visualized in the chromaticity diagram CIE (1931) color coordinates, positions the undoped and Er^{3+} doped nanophosphors in the deep-blue and green light regions, respectively. This study confirms that the prepared nanophosphors hold significant potential for application in the production of visible blue and green LEDs for optical display devices and solid-state lighting applications.

Declaration of Competing Interest

The authors declare that they do not have any identifiable conflicting financial interests or personal connections that might have seemed to impact the research presented in this article.

Data Availability

Data will be made available on request.

Acknowledgements

The authors thank the Consejo Nacional de Umanidades Ciencias y Tecnologías (CONAHCyT) in Mexico for the financial support of the Ph. D. Research Grants [Ref. No.: 1114163] to Nathan Akache Abutu. To the staff at Centro de Investigación en Materiales Avanzados, S.C. Mexico for the characterization and analysis. In addition, we thank the Department of Physics, Federal Agricultural University of Makurdi, Nigeria, for their encouragement of this research work.

References

- [1] P.P. Sukul, M.K. Mahata, U.K. Ghorai, K. Kumar, Crystal phase induced upconversion enhancement in $\text{Er}^{3+}/\text{Yb}^{3+}$ doped SrTiO_3 ceramic and its temperature sensing studies, *Spectrochim. Acta A Mol. Biomol. Spectrosc.* 212 (2019) 78–87, <https://doi.org/10.1016/j.saa.2018.12.039>.
- [2] E. Li, W. Ma, P. Zhang, C. Zhang, Y. Bai, H. Liu, S. Yan, H. Dong, X. Meng, The effect of Al^{3+} doping on the infrared radiation and thermophysical properties of SrZrO_3 perovskites as potential low thermal infrared material, 116795–11, *Acta Mater.* 209 (2021), <https://doi.org/10.1016/j.actamat.2021.116795>.
- [3] H. Lim, J. Lim, S. Jang, Y.S. Lee, Emissions of Er^{3+} and Yb^{3+} co-doped SrZrO_3 nanocrystals under near-infrared and near-ultraviolet excitations, *J. Adv. Ceram.* 9 (2020) 413–423, <https://doi.org/10.1007/s40145-020-0381-x>.
- [4] Y. Liu, Y. Bai, E. Li, Y. Qi, C. Liu, H. Dong, R. Jia, W. Ma, Preparation and characterization of $\text{SrZrO}_3\text{-La}_2\text{Ce}_2\text{O}_7$ composite ceramics as a thermal barrier coating material, 122904–7, *Mater. Chem. Phys.* 247 (2020), <https://doi.org/10.1016/j.matchemphys.2020.122904>.
- [5] S.N. Shkerin, A.V. Rudakova, K.M. Bulanin, A.S. Khaliullina, A.N. Meshcherskikh, E.G. Vovkotrub, L.A. Dunyushkina, Raman spectroscopy of SrZrO_3 based proton conducting electrolyte: Effect of Y-doping and Sr-nonstoichiometry, *Int. J. Hydrog. Energy* 46 (2021) 17007–17018, <https://doi.org/10.1016/j.ijhydene.2020.11.236>.
- [6] A. Kumar, S. Kumari, H. Borkar, R.S. Katiyar, J.F. Scott, Experimental verification of the ab initio phase transition sequence in SrZrO_3 and comparisons with SrHfO_3 and SrSnO_3 , *NPJ Comput. Mater.* 3 (1) (2017) 6, <https://doi.org/10.1038/s41524-016-0002-y>.
- [7] A. Nathan-Abutu, I. Ahemen, A. Reyes-Rojas, Structural and optical investigation of novel $\text{Sr}_{1-x}\text{Na}_x\text{ZrO}_3$ perovskite nanoparticles, 414655–11, *Phys. B Condens Matter* 653 (2023), <https://doi.org/10.1016/j.physb.2023.414655>.
- [8] M.A. Hassairi, A. Garrido Hernández, M. Dammak, D. Zambon, G. Chadeyron, R. Mahiou, Tuning white upconversion emission in $\text{GdPO}_4:\text{Er}/\text{Yb}/\text{Tm}$ phosphors, *J. Lumin.* 203 (2018) 707–713, <https://doi.org/10.1016/j.jlumin.2018.07.024>.
- [9] Q. Xiao, X. Yin, L. Lv, X. Dong, N. Zhou, K. Liu, X. Luo, White up-conversion luminescence and highly-sensitive optical temperature sensing in $\text{Na}_3\text{La}(\text{VO}_4)_2:\text{Yb}$, Er , Tm , Ho phosphors, *J. Rare Earths* (2022) 981–988, <https://doi.org/10.1016/j.jre.2022.04.013>.
- [10] Sheetal, V.B. Taxak, R. Arora, Dayawati, S.P. Khatkar, Synthesis, structural and optical properties of $\text{SrZrO}_3:\text{Eu}^{3+}$ phosphor, *J. Rare Earths* 32 (2014) 293–297, [https://doi.org/10.1016/S1002-0721\(14\)60070-3](https://doi.org/10.1016/S1002-0721(14)60070-3).
- [11] P. Citbor, After-glow luminescence of SrZrO_3 prepared by plasma spraying, *Boletín. De. La Soc. Española De. Cerámica Y. Vidr.* 57 (2018) 190–194, <https://doi.org/10.1016/j.bseccv.2018.04.001>.
- [12] T.J. Pérez-Juache, R. López-Juárez, E. Barrera-Calva, F. González, Luminescent properties of Pr^{3+} -doped SrZrO_3 phosphors, *J. Lumin.* 192 (2017) 599–607, <https://doi.org/10.1016/j.jlumin.2017.07.048>.
- [13] W. Costa Macedo, A. Germano Bispo Junior, K. de Oliveira Rocha, A.E. de Souza Albas, A.M. Pires, S. Rainho Teixeira, E. Longo, Photoluminescence of Eu^{3+} -doped CaZrO_3 red-emitting phosphors synthesized via microwave-assisted hydrothermal method, 100966–8, *Mater. Today Commun.* 24 (2020), <https://doi.org/10.1016/j.mtcomm.2020.100966>.
- [14] Y.Q. Jia, Crystal radii and effective ionic radii of the rare earth ions, *J. Solid State Chem.* 95 (1991) 184–187, [https://doi.org/10.1016/0022-4596\(91\)90388-X](https://doi.org/10.1016/0022-4596(91)90388-X).
- [15] P. Redhu, R. Punia, A. Hooda, B.P. Malik, G. Sharma, P. Sharma, Correlation between multifunctional properties of lead free iron doped BCT perovskite ceramics, *Ceram. Int* 46 (2020) 17495–17507, <https://doi.org/10.1016/j.ceramint.2020.04.045>.
- [16] Jun Ho Kim, Jeong Woo Yun, Sulfur Tolerance Effects on $\text{Sr}_{0.92}\text{Y}_{0.08}\text{Ti}_{0.5}\text{Fe}_{0.5}\text{O}_{3-\delta}$ as an Alternative Anode in Solid Oxide Fuel Cells, *J. Electrochem. Sci. Technol.* 9 (2018) 133–140, <https://doi.org/10.5229/JECST.2018.9.2.133>.
- [17] F.T.L. Muniz, M.A.R. Miranda, C. Morilla dos Santos, J.M. Sasaki, The Scherrer equation and the dynamical theory of X-ray diffraction, *Acta Crystallogr. A Found. Adv.* 72 (2016) 385–390, <https://doi.org/10.1107/S205327331600365X>.
- [18] O. Kalu, A.N. Abutu, H. Esparza Ponce, A. Ramirez-DelaCruz, R.E. Kroon, A. Reyes-Rojas, Structural and optical characterization of RF sputtered CdMgZnO thin film with different Cd concentrations, 128314–11, *Mater. Chem. Phys.* 308 (2023), <https://doi.org/10.1016/j.matchemphys.2023.128314>.
- [19] A. Nathan, J. Rex, A. Roy, Luminescence Characteristics of Polymer Passivized Strontium Aluminate Phosphor, *Phys. Sci. Int. J.* 8 (2015) 1–6, <https://doi.org/10.9734/PSIJ/2015/20601>.
- [20] X. Luo, R. Hu, S. Liu, K. Wang, Heat and fluid flow in high-power LED packaging and applications, *Prog. Energy Combust. Sci.* 56 (2016) 1–32, <https://doi.org/10.1016/j.pecs.2016.05.003>.
- [21] J. Militký, Fundamentals of soft models in textiles. in: *Soft Computing in Textile Engineering*, Elsevier, 2011, pp. 45–102, <https://doi.org/10.1533/9780857090812.1.45>.
- [22] R. Alcaraz de la Osa, I. Iparraguirre, D. Ortiz, J.M. Saiz, The extended Kubelka–Munk theory and its application to spectroscopy, *ChemTexts* 6 (1) (2020) 14, <https://doi.org/10.1007/s40828-019-0097-0>.
- [23] R. Borja-Urby, L.A. Diaz-Torres, P. Salas, C. Angeles-Chavez, O. Meza, Strong broad green UV-excited photoluminescence in rare earth ($\text{RE}=\text{Ce}$, Eu , Dy , Er , Yb) doped barium zirconate, *Mater. Sci. Eng.: B* 176 (2011) 1388–1392, <https://doi.org/10.1016/j.mseb.2011.03.008>.
- [24] P.R. Jubu, O.S. Obaseki, A. Nathan-Abutu, F.K. Yam, Y. Yusof, M.B. Ochang, Dispensability of the conventional Tauc's plot for accurate bandgap determination from UV–vis optical diffuse reflectance data, 100273–7, *Results Opt.* 9 (2022), <https://doi.org/10.1016/j.rso.2022.100273>.
- [25] S.S.A. Gillani, R. Ahmad, M. Rizwan, M. Rafique, G. Ullah, C.B. Cao, H.B. Jin, Effect of magnesium doping on band gap and optical properties of SrZrO_3 perovskite: A first-principles study, *Opt. (Stuttg.)* 191 (2019) 132–138, <https://doi.org/10.1016/j.ijleo.2019.05.099>.
- [26] M. Yaseen, H. Shafiq, J. Iqbal, Misbah, F. Batool, A. Murtaza, M. Iqbal, H. Althib, S. M. Ramay, A. Mahmood, Pressure induced electronic, optical and thermoelectric properties of cubic SrZrO_3 : DFT investigation, 412626–8, *Phys. B Condens Matter* 612 (2021), <https://doi.org/10.1016/j.physb.2020.412626>.
- [27] X.B. Lu, G.H. Shi, J.F. Webb, Z.G. Liu, Dielectric properties of SrZrO_3 thin films prepared by pulsed laser deposition, *Appl. Phys. A* 77 (2003) 481–484, <https://doi.org/10.1007/s00339-002-1469-6>.
- [28] L.S. Cavalcante, A.Z. Simões, J.C. Sczancoski, V.M. Longo, R. Erlo, M.T. Escote, E. Longo, J.A. Varela, SrZrO_3 powders obtained by chemical method: synthesis, characterization and optical absorption behaviour, *Solid State Sci.* 9 (2007) 1020–1027, <https://doi.org/10.1016/j.solidstatesciences.2007.07.019>.
- [29] Z. Guo, B. Sa, B. Pathak, J. Zhou, R. Ahuja, Z. Sun, Band gap engineering in huge-gap semiconductor SrZrO_3 for visible-light photocatalysis, *Int. J. Hydrog. Energy* 39 (2014) 2042–2048, <https://doi.org/10.1016/j.ijhydene.2013.11.055>.

- [30] M. Sultan, T. Miyazaki, S. Koyama, Optimization of adsorption isotherm types for desiccant air-conditioning applications, *Renew. Energy* 121 (2018) 441–450, <https://doi.org/10.1016/j.renene.2018.01.045>.
- [31] Rahman Muttakin, Pal Shafuallah, Saha, A Statistical Approach to Determine Optimal Models for IUPAC-Classified Adsorption Isotherms, 4565–34, *Energy* 12 (2019), <https://doi.org/10.3390/en12234565>.
- [32] S. Lowell, J.E. Shields, M.A. Thomas, M. Thommes, *Characterization of porous solids and powders: surface area, pore size and density*, Springer Science & Business Media, Netherlands, 2006.
- [33] N. Ding, S.W. Chien, T.S.A. Hor, R. Lum, Y. Zong, Z. Liu, Influence of carbon pore size on the discharge capacity of Li–O₂ batteries, *J. Mater. Chem. A* 2 (2014) 12433–12441, <https://doi.org/10.1039/C4TA01745E>.
- [34] S. Li, X. Tan, H. Li, Y. Gao, Q. Wang, G. Li, M. Guo, Investigation on pore structure regulation of activated carbon derived from sargassum and its application in supercapacitor, 10106–17, *Sci. Rep.* 12 (2022), <https://doi.org/10.1038/s41598-022-14214-w>.
- [35] M. Tarrida, H. Languem, M. Madon, Structural investigations of (Ca,Sr)ZrO₃ and Ca (Sn,Zr)O₃ perovskite compounds, *Phys. Chem. Min.* 36 (2009) 403–413, <https://doi.org/10.1007/s00269-008-0286-7>.
- [36] L. Dunyushkina, A. Khaliullina, A. Meshcherskikh, A. Pankratov, D. Osinkin, Effect of A-site nonstoichiometry on defect chemistry and electrical conductivity of undoped and Y-doped SrZrO₃, *Materials* 12 (2019), <https://doi.org/10.3390/ma12081258>.
- [37] W. Shahzad, A.K. Badawi, Z.A. Rehan, A.M. Khan, R.A. Khan, F. Shah, S. Ali, B. Ismail, Enhanced visible light photocatalytic performance of Sr_{0.3}(Ba,Mn)_{0.7}ZrO₃ perovskites anchored on graphene oxide, *Ceram. Int* 48 (2022) 24979–24988, <https://doi.org/10.1016/j.ceramint.2022.05.151>.
- [38] A. Khaliullina, A. Meshcherskikh, A. Pankratov, L. Dunyushkina, Effect of Sr deficiency on electrical conductivity of Yb-doped strontium zirconate, *Materials* 15 (2022), <https://doi.org/10.3390/ma15124126>.
- [39] S. Ni, X. Yang, T. Li, Hydrothermal synthesis and photoluminescence properties of SrCO₃, *Mater. Lett.* 65 (2011) 766–768, <https://doi.org/10.1016/j.matlet.2010.11.056>.
- [40] W.G. Stirling, Neutron inelastic scattering study of the lattice dynamics of strontium titanate: harmonic models, *J. Phys. C: Solid State Phys.* 5 (1972) 2711–2730, <https://doi.org/10.1088/0022-3719/5/19/005>.
- [41] R. Migoni, K.H. Rieder, K. Fischer, H. Bilz, Lattice dynamics and Raman spectra of SrTiO₃, *Ferroelectrics* 13 (1976) 377–379, <https://doi.org/10.1080/00150197608236617>.
- [42] G. Pezzotti, A.A. Porporati, Raman spectroscopic analysis of phase-transformation and stress patterns in zirconia hip joints, *J. Biomed. Opt.* 9 (2004) 372–384, <https://doi.org/10.1117/1.1647547>.
- [43] T.M. Arantes, G.P. Mambrini, D.G. Stroppa, E.R. Leite, E. Longo, A.J. Ramirez, E. R. Camargo, Stable colloidal suspensions of nanostructured zirconium oxide synthesized by hydrothermal process, *J. Nanopart. Res.* 12 (2010) 3105–3110, <https://doi.org/10.1007/s11051-010-9906-5>.
- [44] H. Zheng, G.D.C. Csete de Györgyfalva, R. Quimby, H. Bagshaw, R. Ubbel, I. M. Reaney, J. Yarwood, Raman spectroscopy of B-site order–disorder in CaTiO₃-based microwave ceramics, *J. Eur. Ceram. Soc.* 23 (2003) 2653–2659, [https://doi.org/10.1016/S0955-2219\(03\)00149-3](https://doi.org/10.1016/S0955-2219(03)00149-3).
- [45] M.M. Rashad, A.G. Mostafa, D.A. Rayan, Structural and optical properties of nanocrystalline mayenite Ca₁₂Al₁₄O₃₃ powders synthesized using a novel route, *J. Mater. Sci.: Mater. Electron.* 27 (2016) 2614–2623, <https://doi.org/10.1007/s10854-015-4067-z>.
- [46] K. Sedeek, N. Makram, H. Hantour, T.Z. Amer, S.A. Said, An explicit and novel structure, lattice dynamics, and photoemission of La-doped nanocrystalline SrZrO₃ perovskite, *Rare Met.* 40 (2021) 105–112, <https://doi.org/10.1007/s12598-019-01326-y>.
- [47] T. Tiittanen, M. Karppinen, Kinetics and thermodynamics of B-site cation order in (Sr,Ba)₂FeSbO₆ perovskite, *J. Solid State Chem.* 258 (2018) 11–14, <https://doi.org/10.1016/j.jssc.2017.09.032>.
- [48] J.W. Park, D.J. Lee, D.H. Kim, Y. Lee, Low-temperature Photoluminescence for Polycrystalline SrZrO₃ and SrHfO₃, *J. Korean Phys. Soc.* 58 (2011) 316–320, <https://doi.org/10.3938/jkps.58.316>.
- [49] D.J. Lee, D.H. Kim, J.W. Park, Y.S. Lee, Room-temperature violet-blue emission for SrZrO₃ nanocrystals synthesized by using the combustion method, *J. Korean Phys. Soc.* 59 (2011) 2797–2800, <https://doi.org/10.3938/jkps.59.2797>.
- [50] I. Ahemen, F.B. Dejene, R.E. Kroon, H.C. Swart, Effect of europium ion concentration on the structural and photoluminescence properties of novel Li₂BaZrO₄:Eu³⁺ nanocrystals, *Opt. Mater. (Amst.)* 74 (2017) 58–66, <https://doi.org/10.1016/j.optmat.2017.03.029>.
- [51] G. Blasse, Energy transfer in oxide phosphors, *Phys. Lett. A* 28 (1968) 444–445, [https://doi.org/10.1016/0375-9601\(68\)90486-6](https://doi.org/10.1016/0375-9601(68)90486-6).
- [52] L. Li, Y. Pan, Z. Chen, S. Huang, M. Wu, Tunable luminescence and energy transfer properties of Bi³⁺ and Mn⁴⁺ co-doped Ca₁₄Al₁₀Zn₆O₃₅ phosphors for agricultural applications, *RSC Adv.* 7 (2017) 14868–14875, <https://doi.org/10.1039/C7RA01285C>.
- [53] J. Li, Z. Wu, X. Sun, X. Zhang, R. Dai, J. Zuo, Z. Zhao, Controlled hydrothermal synthesis and luminescent properties of Y₂WO₆:Eu³⁺ nanophosphors for light-emitting diodes, *J. Mater. Sci.* 52 (2017) 3110–3123, <https://doi.org/10.1007/s10853-016-0598-9>.
- [54] I. Ahemen, F.B. Dejene, Site spectroscopy probing of Eu³⁺ incorporated into novel LiYrZrO_{3+α} host matrix, *Curr. Appl. Phys.* 18 (2018) 1359–1367, <https://doi.org/10.1016/j.cap.2018.07.021>.
- [55] S. Taherunnisa, D.V.K. Reddy, T. SambasivaRao, K.S. Rudramamba, Y. A. Zhyachevskyy, A. Suchocki, M. Piasecki, M.R. Reddy, Effect of up-conversion luminescence in Er³⁺ doped phosphate glasses for developing Erbium-Doped Fibre Amplifiers (EDFA) and G-LED's, 100034–11, *Opt. Mater.: X* 3 (2019), <https://doi.org/10.1016/j.omx.2019.100034>.
- [56] C. Li, G. Cui, M. Melgosa, X. Ruan, Y. Zhang, L. Ma, K. Xiao, M.R. Luo, Accurate method for computing correlated color temperature, *Opt. Express* 24 (13) (2016) 14066, <https://doi.org/10.1364/OE.24.014066>.
- [57] C.S. McCamy, Correlated color temperature as an explicit function of chromaticity coordinates, *Color Res Appl.* 17 (1992) 142–144, <https://doi.org/10.1002/col.5080170211>.
- [58] S.-M. Moon, S.-Y. Kwon, J.-H. Lim, Implementation of smartphone-based color temperature and wavelength control LED lighting system, *Clust. Comput.* 19 (2016) 949–966, <https://doi.org/10.1007/s10586-016-0548-y>.
- [59] R. Zhang, Z. Wen, B. Li, S. Liang, M. Yang, Z. Xia, Research on COB-LED light source with tunable CCT based on screen printing and flip chip technology, *Opt. Quantum Electron* 54 (2022) 79, <https://doi.org/10.1007/s11082-021-03466-x>.